Journal Pre-proofs

Biomimic FeS_2 Nanodrug with Hypothermal Photothermal Effect by Clinical Approved NIR-II Light for Augmented Chemodynamic Therapy

Dejun She, Shaojun Peng, Li Liu, Huihui Huang, Yingyan Zheng, Yiping Lu, Daoying Geng, Bo Yin

PII: S1385-8947(20)32061-1
DOI: https://doi.org/10.1016/j.cej.2020.125933
Reference: CEJ 125933

To appear in: *Chemical Engineering Journal*

Received Date: 3 March 2020
Revised Date: 4 June 2020
Accepted Date: 16 June 2020

Please cite this article as: D. She, S. Peng, L. Liu, H. Huang, Y. Zheng, Y. Lu, D. Geng, B. Yin, Biomimic FeS_2 Nanodrug with Hypothermal Photothermal Effect by Clinical Approved NIR-II Light for Augmented Chemodynamic Therapy, *Chemical Engineering Journal* (2020), doi: https://doi.org/10.1016/j.cej.2020.125933

Biomimic FeS_2 Nanodrug with Hypothermal Photothermal Effect by Clinical Approved NIR-II Light for Augmented Chemodynamic Therapy

Dejun She[a,1], Shaojun Peng[b,1,*], Li Liu[c], Huihui Huang[d], Yingyan Zheng[a], Yiping Lu[a], Daoying Geng*[a], Bo Yin*[a,e]

[a] Department of Radiology, Huashan Hospital, Fudan University, Shanghai, 200040, PR China

[b] Zhuhai Precision Medical Center, Zhuhai People's Hospital (Zhuhai hospital affiliated with Jinan University), Zhuhai, 519000, Guangdong, PR China

[c] Department of Radiology, Fudan University Shanghai Cancer Center, Shanghai, 200030, PR China

[d] Department of Pharmacology, College of Pharmacy, Fujian Medical University, Fuzhou, 350122, Fujian, PR China

[e] Department of Radiology, Huashan Hospital North, Fudan University, Shanghai, 201907, PR China

[1] Contributed equally to this work

[*] Corresponding author

E-mail: henry2008_ok@126.com (S. Peng), gengdaoying@126.com (D. Geng) and yinbo@fudan.edu.cn (B. Yin).

ABSTRACT

Hypothermal photothermal therapy (HPTT) employs hyperthermia (<45 °C) to destroy tumor cells with negligible side effects to the surrounding normal tissues. Despite extensive studies, the clinical translation of HPTT is severely hindered, owing to the discounted therapeutic effect and maximum permissible power of near-infrared (NIR) laser by food and drug administration (FDA). Herein, we report a rational design of red blood cell membranes (RBCs) coated FeS_2 (FeS_2@RBCs) with strong absorption at NIR-II window for effective HPTT augmented chemodynamic therapy (CDT). FeS_2@RBCs exhibits prolonged blood circulation and negligible immune response, leading to improved tumor accumulation for enhanced HPTT. Furthermore, the CDT effect of FeS_2@RBCs is significantly augmented by the temperature elevation in the tumor region, which leads to the synergetic HPTT and CDT. Lipidomics analysis reveals that the damage of tumor cells by CDT is *via* the lipid peroxidation. In addition, FeS_2@RBCs exhibits self-enhanced magnetic resonance imaging after reacting with H_2O_2 in tumor region for imaging-guided laser irradiation. Thus, FeS_2@RBCs achieves remarkable inhibition of subcutaneous 4T1 breast tumor growth without obvious side effects by a 1064 nm laser irradiation of 1.0 W/cm^2 (FDA approved power density). Overall, this work provides a HPTT augmented CDT strategy for effective cancer therapy with a clinical approved laser power, which may pave the way for the clinical application of HPTT augmented CDT in the future.

Keywords: RBC membranes, hypothermal photothermal therapy, chemodynamic therapy, self-enhanced imaging, NIR-II Light

1. Introduction

As a promising alternative to cancer traditional therapy, photothermal therapy (PTT) has been considered as a noninvasiveness and tumor-selective therapeutic modality[1-3]. Notably, hypothermal photothermal therapy (HPTT), which employs hyperthermia (<45 °C) to destroy tumor cells with negligible side effects to the surrounding normal tissues, has attracted widespread attention recently[4-7]. Despite extensive researches, the further clinical translation and application of HPTT are seriously hindered, mainly owing to the discounted therapeutic effect and low maximum permissible exposure (MPE) of NIR laser in clinical use [8-13]. According to the criterions of food and drug administration (FDA), the clinical approved MPE for skin exposure is 1.0 W/cm^2 for the 1064 nm laser and 0.33 W/cm^2 for 808 nm laser [14,15]. Therefore, how to implement efficient HPTT under the FDA-approved laser power has become an urgent issue. Recent studies in the laser wavelength for effective HPTT have attempted to replace the conventional NIR-I optical window with the second NIR (NIR-II) optical window (1000–1700 nm), since the NIR-II spectral region allows the higher MPE and expected maximum penetration depth of tissue [16-20]. Yet the work in the NIR-II optical window with satisfactory HPTT efficiency under the FDA-approved laser power density is still at an infancy stage.

It has been demonstrated that increasing the blood circulation time of photothermal agents could enhance their tumor accumulation, thereby significantly improving the PTT efficiency [21-23]. Although polyethylene glycol (PEG) coating has been regarded as the gold standard strategy to prolong the blood circulation of photothermal agents, it still shows rapid clearance from blood, leading to unsatisfactory tumor accumulation [24,25]. Very recently, utilization of nature cell membrane for photothermal agents coating through a top-down approach has been recognized as a superior alternative [26-29]. Affording prolonged blood circulation, red blood cell membranes (RBCs) have been proposed as an excellent coating to deliver various photothermal agents to tumor tissues [23,30]. RBCs with natural surface makeup comprising of "self-marker" (e.g., CD47 protein, various peptides, acidic sialyl moieties and glycans) could significantly inhibit nonspecific macrophage phagocytosis and prolong blood circulation *in vivo* [31]. For example, RBCs-camouflaged Fe_3O_4 nanoparticles have been proved to exhibit improved tumor accumulation compared to bare Fe_3O_4 nanoparticles, leading to superior PTT efficiency [23]. Therefore, it is an effective way to extend the blood circulation of photothermal agent by RBCs coating, thereby enhancing the therapeutic efficiency and reducing the necessary laser power density in HPTT.

Another way to strengthen the therapeutic efficiency of HPTT is to develop the combined therapy. Chemodynamical therapy (CDT), which typically relies on iron-mediated Fenton reaction to induce cancer cell ferroptosis by catalyzing non-toxic hydrogen peroxide (H_2O_2) into highly toxic hydroxyl radicals (·OH), is an emerging anti-tumor strategy [32-35]. Importantly, ·OH is generated only in a tumor-specific environment without harming normal tissues because of the higher concentration of H_2O_2 in tumor microenvironment (TME) (~100 μM) than that in normal tissues [36]. However, the therapeutic effect of CDT is far from satisfactory, which is restricted by the concentration of H_2O_2 and low Fenton reaction efficiency in the TME. It has been showed that the temperature elevation in the tumor region could substantially improve the Fenton reaction efficiency and ·OH productivity [37-38]. Therefore, the rational combination of HPTT and CDT are expected to substantially improve the overall therapeutic efficacy, hence overcoming the obstacle of high laser density utilization in HPTT.

Imaging-assisted tumor therapy is a promising approach to improve the performance of cancer therapy, which could achieve precise location of tumors for highly localized treatments [39-43]. Imaging-assisted PTT can significantly improve photothermal efficacy and simultaneous reduce the laser power for PTT by quantifying photothermal agents within tumor at the appropriate time point [44-46]. Magnetic resonance imaging (MRI), as a noninvasive molecular imaging technique, has been extensively used in imaging-assisted cancer therapy due to its excellent anatomic detail of high spatial resolution, high soft-tissue image contrast, and no penetration depth constraints without radiation risk [47,48]. Recently, ferrous ion-based nanoparticle, as a self-enhanced MRI contrast agent, has attracted widespread attention in real-time visualizing drug accumulation and monitoring treatment [49,50]. Accordingly, it is highly desirable to assemble self-enhanced MR imaging into photothermal agents for MRI-guided HPTT.

Herein, we report a rational design of RBCs coated FeS_2 (FeS_2@RBCs) for TME-enhanced MRI-guided HPTT and CDT for cancer synergetic therapy, as shown in Fig. 1. Firstly, FeS_2@RBCs offers strong adsorption at NIR-II window, superior blood circulation and improved tumor accumulation for effective cancer HPTT. Furthermore, the CDT effect of FeS_2@RBCs is accelerated simultaneously by the hyperthermia for a synergistic HPTT/CDT therapy. Additionally, the TME-enhanced MRI could visualize the nanoparticle accumulation within tumor region for pretreatment guidance. According to the results of *in vitro* and *in vivo* experiments, FeS_2@RBCs realizes pronounced cancer therapeutic efficiency with a FDA-approved laser power density (1.0 W/cm^2 for 1064 nm), which may pave the way for the application of synergetic HPTT and CDT in clinical use.

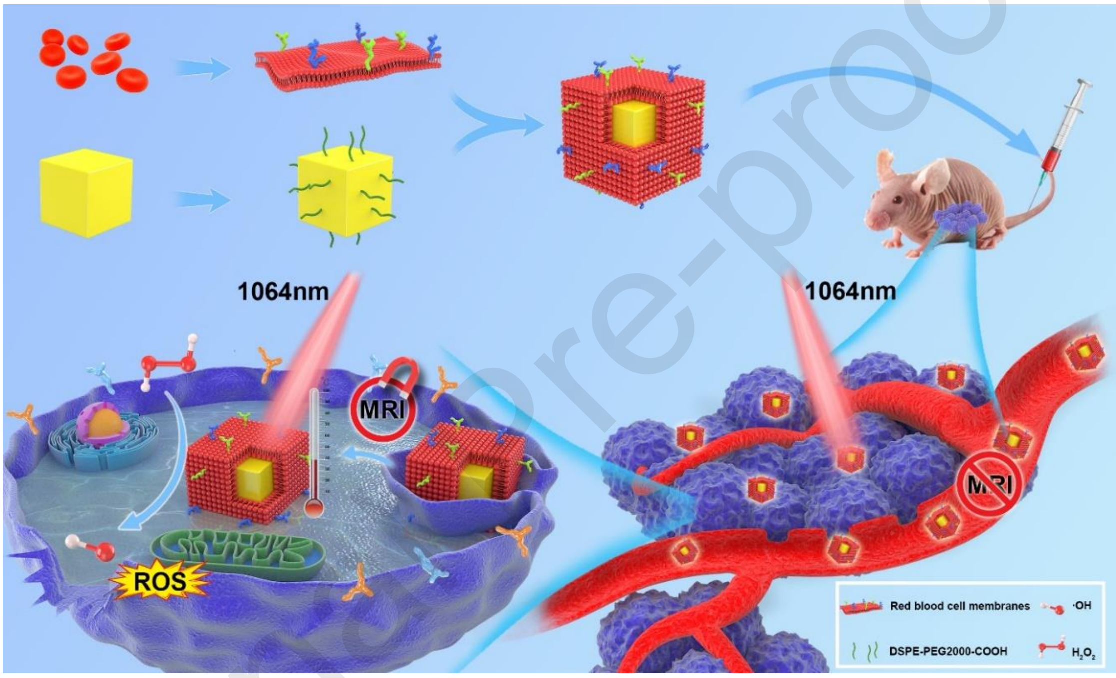

Fig. 1. Schematic illustrating the fabrication and anti-tumor effect of FeS_2@RBCs *in vivo*. With RBCs coating, FeS_2@RBCs exhibits prolonged blood circulation, which leads to the improved tumor accumulation. FeS_2@RBCs shows TME-enhanced MRI after reacting with H_2O_2 at tumor regions for imaging-guided HPTT. With a FDA approved 1064 nm laser, FeS_2@RBCs achieves effective HPTT, which significantly augments the CDT effects for tumor synergetic therapy. The growth of tumor could be significantly inhibited by a clinical approved NIR-II laser.

2. Materials and methods

2.1.Materials

Iron dichloride (99%), Oleylamine (80%-90%), 1-Dodecanethiol, Sulfur powder (99.95%), hydrogen peroxide (H_2O_2, 30%) are ordered from Aladdin (Shanghai, China). DSPE-PEG2000, 3,3',5,5'-Tetramethylbenzidine dihydrochloride (TMB), methylene blue (MB) and 2,7-dichlorofluorescin diacetate (DCFH-DA) are obtained from Sigma-Aldrich (St. Louis, USA). Dulbecco's modified Eagle medium (DMEM/High glucose), fetal bovine serum (FBS), penicillin-streptomycin solution, and trypsin-Ethylene Diamine Tetraacetic Acid (Trypsin-EDTA, 0.05%) are purchased from Life Science (Gibco™, Pittsburgh, USA). Cell counting kit-8 (CCK-8), Calcein-AM and Propidium Iodide apoptosis detection kit, DAPI, and Cyanine5 amine dye (expressed as Cy5) are from KeyGen Biotech, Co., Ltd (Nanjing, China). Ultrapure water is prepared using Milli-Q water purification system (18.2 MΩ.cm, Millipore, Bedford, MA). All the other chemical agents are purchased from Sinopharm Chemical Reagent (Shanghai, China).

The 4T1 and human embryonic kidney cell line (293T cell line) are purchased from Chinese Academy of Sciences Cell Bank. Balb/c nude mice (female, 6-8 weeks old, 20-22g) are acquired from BK lab (Shanghai, China). All animal experiment procedures are ratified and supervised by the Institutional Animal Care and Use Committee (IACUC) of Fudan University.

2.2.Instruments

Dynamic light scattering (DLS) measurements are performed using a Zetasizer Nano ZS analyzer (Malvern, UK). Transmission Electron Microscope (TEM) images are obtained by using a transmission electron microscope (Tecnai G2 20 TWIN, FEI, USA). X-ray diffraction (XRD) spectra is recorded on a Bruker D8 ADVANCE diffractometer

(Germany) with Cu Kα (λ = 1.5406 Å). X-ray photoelectron spectra (XPS) measurements are performed applying an ESCA-Lab-200i-XL spectrometer with monochromatic Al Kα radiation (1486.6 eV). UV-vis spectrum is performed with a Lamba 750 spectrophotometer (Perkin Elmer, Boston, MA). To get confocal laser scanning microscopy (CLSM) images, a Nikon C^{2+} laser scanning confocal microscope (Nikon, Japan) are applied. The MR images are performed by using a 3T MR imaging system (GE 750, GE, USA) with a 8-channel head coil and a 3T MR imaging system (Magnetom Verio, Siemens, Germany) with a 4-channel mice coil. Photothermal effect is tested on a 1064 nm consecutive NIR laser or a 808 nm consecutive NIR laser (New Industries Optoelectronics Technology Co., Ltd, China), respectively. Thermal images are performed with a thermal infrared camera (InfraTec, VarioCAM hr research, Germany). Confocal laser scanning microscopy (CLSM) images are acquired on FV1000 (Olympus Company, Japan).

2.3. Synthesis and Characterization of FeS_2@RBCs

In briefly, 3 mmol sulfur powders and 0.5 mmol iron (II) chloride are dissolved in 15 mL oleylamine, followed by the addition of 5 mL of 1-Dodecanethiol under magnetic stirring. After one-hour magnetic stirring for ample dissolution, the mixture is moved to a stainless-steel autoclave, and heated at 180 ^{o}C for 18 h. Afterwards, the black solid products are centrifuged (10000 rpm, 10 min) and washed with hexane for three times. At the last centrifugation, the black solid products are washed with ethyl alcohol and then dissolved in absolute alcohol. FeS_2 is used for further PEGylation by using DSPE-PEG2000, named as FeS_2-PEG, according to the previous study with slight modifications [51].

The preparation approach of RBCs vesicles are derived from our previous published protocol with slight modification [52]. Firstly, the whole blood (1 mL) is taken from Balb/c mice (female, 20-22 g), dispersed in 10 ml phosphate saline buffer solution (1× PBS) containing heparin. Afterwards, the solution is centrifuged at 600 × g for 5 min at 4 ^oC to remove the supernatant and collect RBCs. The RBCs are washed with 1 mM EDTA·2Na-containing PBS (1×, 4 ^oC) for four times and was collected by centrifugation to remove buffy coat and serum. Then, the recollected RBCs are suspended to 0.25 mM EDTA·2Na-containing deionized water (4 ^oC) for hemolysis and centrifuged at 20000 g at 4 ^oC to remove the hemoglobin. Finally, the RBCs vesicle are collected, re-dispersed in PBS, and stored at -80 ^oC for the following experiment.

FeS_2@RBCs are prepared by mixing and sonicating 5 min at 4 ^oC with the surface area ratio ($S_{RBC}/S_{FeS_2\text{-}PEG}$) of 1:1. The resulting mixtures then are centrifuged at 6000 rpm for 10 min and washed with deionized water for two times to eliminate excess RBCs vesicles. The FeS_2@RBCs are restored in PBS for further DLS, TEM, XRD and UV-vis characterization. The hydrodynamic sizes of FeS_2@RBCs are measured for three days in PBS to explore the long-term stability of FeS_2@RBCs in PBS.

The proteins on FeS_2@RBCs are further characterized with sodium dodecyl sulfate-polyacrylamine gel electrophoresis (SDS-PAGE) method. In briefly, the FeS_2-PEG, RBCs vesicles and FeS_2@RBCs are mixed with RIPA lysis buffer and determined by the bicinchoninic acid (BCA) assay kit (Beyotime, China). Subsequently, the sample is heated at 95 ^oC for 5 min, and 40 μg/well of each sample is loaded into 10 % SDS-PAGE gel. The sample is performed at 120 V for 2 h, stained in Coomassie Blue, washed with deionized water for 12 h, and imaged finally. The presence of typical marker of RBCs (CD47 protein), is conducted by using Western blot analysis. The resulting protein is transferred onto a polyvinylidene difluoride membrane. The membrane is incubated with a primary rabbit anti-mouse CD47 antibody for 12 h at 4 ^oC, followed by incubation with a horseradish peroxidase-conjugated goat anti-rabbit IgG secondary antibody for 1 h at 37 ^oC. The protein signals are recorded by enhanced chemiluminescence detection kit using a ChemiDoc™ XRS System (Bio-Rad, USA).

2.4. In vitro and in vivo self-enhanced MRI tests

To test the self-enhanced MRI performance of FeS_2@RBCs in *vitro*, the T_2-weighted signals of FeS_2@RBCs solution at different concentrations with or without H_2O_2 are measured. The FeS_2@RBCs are dissolved into PBS or H_2O_2-containing PBS (100 μM), which are shaken at a speed of 150 rpm at 37 ^oC for 1 h. Subsequently, the FeS_2@RBCs solutions are diluted to the corresponding concentrations (0.25, 0.125, 0.0625, 0.0313, 0.0156 and 0.0078 mM) in 1.5 mL of centrifuge tubes for *in vitro* MR T_2-weighted imaging. T_2-weighted fast-spin-echo (FSE) mapping sequence: TR=3000 ms, TE=14.6/29.2/43.8/58.3/72.9/87.5/102.1/116.7ms, Slice thickness=3.0 mm, gap thickness=3.0 mm, FOV=45mm×80 mm, acquisition matrix=320×280.

To test the self-enhanced MRI performance of FeS_2@RBC *in vivo*, the breast tumor animal model is established by injecting 4T1 cell into the Balb/c nude mice subcutaneously. Firstly, the nude mice are intratumor injected FeS_2@RBCs at a Fe dose of 2 mg/kg and T_2-weighted MRI of 4T1 tumor-bearing mice are performed before and after intra-tumoral injection at predetermined intervals (0, 30, 60, 90 and 120 min). In addition, the nude mice are injected with FeS_2@RBCs at a Fe dose of 2 mg/kg *via* tail vein and T_2-weighted MRI of 4T1 tumor-bearing mice are also performed (0, 2, 4, 6, 12 and 24 h).

2.5. Detection of the specific •OH generation

A commercial chemical agent TMB is employed to detect ·OH generation by recording its UV-vis spectra. In brief, 20 μg of FeS_2@RBCs is dispersed in 1 mL solution containing 0.12 mg TMB, followed by adding 100 μM H_2O_2. In addition, to evaluate photothermal-enhanced effect on the generation of •OH radicals, the aqueous solution containing 20 μg of FeS_2@RBCs and 100 μM H_2O_2 is illuminated by 808 nm (0.33 W/cm^2) or 1064 nm (1.0 W/cm^2) laser for 5 min. Furthermore, MB decolorization of FeS_2@RBCs at different pH values (pH=7.4, 6.5 or 5.5) is explored. Then, UV-vis spectra of each solution are obtained respectively.

DCFH-DA fluorescent probe is employed to assess intracellular generation of ·OH radical. 4T1 cells are planted in confocal dishes (1×10^5 cells/well) and incubated for 24 h. Four groups are established: Control, FeS_2@RBCs, FeS_2@RBCs+808 nm laser (0.33 W/cm^2, 5 min), FeS_2@RBCs+1064 nm laser (1.0 W/cm^2, 5 min). All groups are added with 100 μM H_2O_2. After treatment of 4T1 cells with different formulations, cells are washed three times with PBS and incubated with DMEM containing-DCFH-DA (10 μM) for 30 min. The fluorescence signals of the DCFH-DA fluorescent probe are observed and recorded by CLSM. DCFH-DA staining of tumor slices for saline,

FeS_2@RBCs, FeS_2@RBCs+808 nm laser (0.33 W/cm^2, 5 min) and FeS_2@RBCs+1064 nm laser (1.0 W/cm^2, 5 min) at 2 h post intratumor injection. The nuclei were stained with DAPI.

2.6. Lipidomics analysis

Two groups (6 samples for each group) are set: FeS_2@RBCs and FeS_2@RBCs +1064 nm laser (1.0 W/cm^2, 5 min). Briefly, 4T1 cells treated with different formulations are collected. Five steel balls and 1 mL of MTBE solution (precooled at -20 ^{o}C) are added into centrifuge tubes containing cell samples. The samples are pulverized using a high-flux tissue grinding device (60 Hz, 1.5 min) and subsequently centrifuged for 5 min with a speed of 12000 rpm. Afterwards, the upper layer fluid is transferred into another centrifugal tube and dried by the air blast vacuum drying box. The dried samples are resolved with 200 μL of isopropanol. The final samples are analyzed by liquid chromatography-mass spectrometry (LC-MS).

2.7. In vitro and in vivo photothermal performance of FeS_2@RBCs

To evaluate the photothermal performance of FeS_2@RBCs *in vitro*, 200 μL of FeS_2@RBCs solutions at different concentration (0, 25, 50, 100 μg/mL) are irradiated under a 1064 nm NIR laser (1.0 W/cm^2, 5 min) or at 100 μg/mL under different power densities (0.5. 0.75, 1.0, 1.5 W/cm^2). Meanwhile, FeS_2@RBCs with or without H_2O_2 treatment are irradiated at 100 μg/mL under a 1064 nm NIR laser (1.0 W/cm^2, 5 min). As a control, FeS_2@RBCs at 100 μg/mL is irradiated under a 808 nm NIR laser (0.33 W/cm^2, 5 min). Furthermore, FeS_2-PEG at 100 μg/mL is irradiated under a 1064 nm NIR laser (1.0 W/cm^2, 5 min). Temperature at every 30 s intervals is recorded after irradiation by using an infrared thermal imaging camera. The photothermal efficiency of FeS_2@RBCs under a 1064 nm NIR laser (1.0 W/cm^2, 5 min) is calculated according to the previous literatures [53, 54]. For the photostability tests, the FeS_2@RBCs dispersions are irradiated with the laser (1064 nm, 1.0 W/cm^2) for 5 min and then cooled to the room temperature naturally, which is repeated for 6 times. TEM photographs of FeS_2@RBCs are obtained at the second, the fourth and the sixth cycles of NIR irradiation.

To evaluate the photothermal performance of FeS_2@RBCs *in vivo*, the breast tumor animal model is established by injecting 4T1 cell into the Balb/c nude mice subcutaneously. Firstly, the nude mice are intratumor injected FeS_2@RBCs at a Fe dose of 1 mg/kg, and the tumor regions are irradiated under a 808 nm NIR laser (0.33 W/cm^2, 5 min) or a 1064 nm NIR laser (1.0 W/cm^2, 5 min). Temperature at every 30 s intervals is recorded after irradiation by using an infrared thermal imaging camera.

2.8. In vitro cytocompatibility and therapeutic effect

The cytocompatibility of FeS_2@RBCs are evaluated on 4T1 cells or 293T cells with standard cell counting kit-8 (CCK-8) method. Two cell lines are seeded on 96-well cell culture plates at a density of 1×10^4/well and incubated for 24 h, respectively. Subsequently, cells are treated with FeS_2@RBCs at various concentrations (12.5, 25, 50, 100, 200 μg/mL) for 24 h. Afterwards, the DMEM medium is replaced and CCK-8/culture medium is added to evaluated the cells viability.

In this part, DSPE-PEG-Cy5 is empolyed to modify with FeS_2 to endow the obtained FeS_2-PEG with fluorescent dye. Also, RBCs is coated onto the surface of Cy5 modified

FeS_2-PEG, thereby generating the Cy5 modifed FeS_2@RBCs. 4T1 cells are incubated with Cy5 modifed FeS_2@RBCs (50 μg/mL) and CLSM is applied to observe the cellular uptake behaviors of Cy5 modifed FeS_2@RBCs by 4T1 cells.

4T1 cells are planted on 96-well cell culture plates at a density of 1×10^4/well and incubated for 24 h. The cells are treated with the DMEM medium with 50 or 100 μM H_2O_2 containing FeS_2@RBCs at varying concentrations (0, 25, 50, 100 μg/mL), respectively. Furthermore, the cells are also treated with the DMEM medium with 100 μM H_2O_2 containing FeS_2@RBCs at varying concentrations (0, 25, 50, 100 μg/mL) irradiated by 808 nm (0.33 W/cm^2, 5 min) or 1064 nm laser (1.0 W/cm^2, 5 min), respectively. After additional incubation, the CCK-8/culture medium is added to evaluated the cells viability.

The cell apoptosis-inducing activity of different formulations is qualitatively assessed by using Calcein-AM/PI apoptosis detection assay. 4T1 cells are planted in confocal dishes (1×10^5 cells/well) and incubated for 24 h. Then cells are divided into six groups randomly: Control (100 μM H_2O_2) group, FeS_2@RBCs group, FeS_2@RBCs (100 μM H_2O_2) group, FeS_2@RBCs+1064 nm laser (1.0 W/cm^2, 5 min) group, FeS_2@RBCs+808 nm laser (0.33 W/cm^2, 5 min, 100 μM H_2O_2) group and FeS_2@RBCs+1064 nm laser (1.0 W/cm^2, 5 min, 100 μM H_2O_2) group. After treatment, cells are stained with PBS containing 10 mM of Calcein-AM and 2 mM of PI for 15 min. The cells are imaged on the CLSM.

2.9. Pharmacokinetics and biodistribution studies

Then, the Balb/c nude mice are randomly injected with 100 μL of Cy5 modified FeS_2-PEG or FeS_2@RBCs at a Fe concentration of 0.4 mg/mL *via* the tail vein, respectively. At different time point following the administration, 100 μL of blood are derived from the mouse orbital plexus. The nanoparticle concentrations of blood samples are assessed quantitatively by microplate reader (λ_{ex}=649nm, λ_{em}=670nm).

In biodistribution study, the breast tumor animal model is established as described above. When tumor volume reached approximately 100 mm^3, the tumor-bearing mice are randomly injected with 100 μL of Cy5 modified FeS_2-PEG or FeS_2@RBCs at a Fe concentration of 0.4 mg/mL *via* the tail vein, respectively. The mice are euthanized and followed by heart perfusion at 6 and 24 h after administration. Subsequently, the subcutaneous tumor and major organs including heart, liver, spleen, lungs and kidneys are taken, weighted, and homogenized. The nanoparticle concentrations of tissue samples are evaluated quantitatively by microplate reader (λ_{ex}=649nm, λ_{em}=670nm).

2.10. Anti-cancer therapy in vivo

The breast tumor animal model is established as described above. When tumor volume reached approximately 100 mm^3, the mice are randomly divided into six groups to receive different treatments: Control group, FeS_2-PEG group, FeS_2@RBCs group, FeS_2-PEG +808nm laser group (0.33 W/cm^2, 5 min), FeS_2@RBCs+808nm laser group (0.33 W/cm^2, 5 min), FeS_2@RBCs+1064nm laser group (1.0 W/cm^2, 5 min). For Control group, the tumor-bearing mice are injected saline *via* intravenous injection. For other groups, the mice are intravenously injected with nanoparticles at a Fe dose of 3 mg/kg, respectively. The tumor-bearing mice are irradiated after 6 h administration.

The body weight and tumor volume of the tumor-bearing mice are recorded every other day. The temperature elevation of tumors is imaged by an NIR camera. At 15 days after therapy administration, all the mice are sacrificed, and the tumors and major organs are taken. The tumors and major organs are fixed with 4 % paraformaldehyde for 48 h, embedded in paraffin, sectioned into slices, and stained with terminal-deoxynucleoitidyl transferase mediated nick end labeling (TUNEL) amd hematoxylin and erosin (H&E) staining. At last, the slices are imaged by CLSM.

2.11 Blood biochemistry and blood routine test

To explore the blood compatibility of FeS_2@RBCs, 10 Balb/c mice (~20 g) are randomly divided into two groups as PBS and FeS_2@RBCs. Five of the mice are intravenously injected with 100 μL of FeS_2@RBCs (3 mg/kg) and others are injected with 100 μL of PBS. After the injection for 48 h, blood samples are collected from each mouse for biochemical and routine blood testing.

2.12. Statistical analysis

Statistical analysis was conducted with GraphPad Prism 8 software (USA). One-way analysis of variance (ANOVA) and Tukey's post hoc tests were applied for multiple group comparison. *$P < 0.05$, **$P < 0.01$, and ***$P < 0.001$ was indicated significant, and n.s. represented no significance.

3. Results and discussion

3.1. Fabrication and characterization of FeS_2@RBCs

The procedure for the preparation of FeS_2@RBCs includes following three steps: fabrication of FeS_2-PEG, preparation of RBCs vesicles, and fusion of RBCs on the surface of FeS_2-PEG to obtain the final product FeS_2@RBCs, as illustrated in Fig. 1. Firstly, FeS_2 is fabricated according to a facile solvothermal reaction. From the TEM image, FeS_2 shows the cubic shape with an average diameter of 100-120 nm (Fig. 2a). The selected area electron diffraction (SAED) pattern, HRTEM and XRD demonstrate that the FeS_2 nanoparticles exhibit highly crystalline structure (Fig 2b, Fig. S1 and Fig. S2). SEM image also reveals that the obtained FeS_2 is uniformly dispersed and the composition of FeS_2 is further confirmed by the SEM-EDS mapping (Fig. 2c-e, Fig. S3). The XPS of FeS_2 nanoparticles reveals that the binding energies of 706.9 eV and 719.8 eV are characteristic of FeS_2 nanoparticles, which is attributed to the Fe^{2+} species. Furthermore, the peak at 160.9 eV is assigned to the S^{-1} ions in FeS_2 nanoparticles (Fig. S4). To improve the water dispersibility, DSPE-PEG2000 is employed to modify the FeS_2 by ultrasonic dispersion, generating the FeS_2-PEG. Secondly, RBCs harvested from fresh whole blood are treated with a hypotonic condition to yield RBC membrane vesicles. Lastly, RBCs and FeS_2-PEG are mixed and sonicated for 5 min. The sonication forces facilitate the encapsulation of RBCs onto nanoparticle surfaces effectively, forming the final FeS_2@RBCs. From the TEM image, it is found that an outer membrane shell of around 8.3 nm appear on the surface of FeS_2 inner core after the RBCs coating (Fig. 2f) and the hydrodynamic size of FeS_2@RBCs slightly increases from 168.3 nm (FeS_2-PEG) to 185.2 nm (Fig. 2g). The increased hydrodynamic diameter of 16.9 nm correlated well to the thickness of two layers lipid bilayer of cell membrane. Furthermore, the zeta potential of FeS_2@RBCs is changed from -2.1 mV to -10.3 mV after RBCs coating, owing to the negative charge of RBCs (Fig. 2h). Moreover, UV-vis absorption spectra also exhibit that the FeS_2@RBCs displays a new absorbance peak at 410 nm (Fig. 2i) compared with bare inner FeS_2, which is in identical with that of RBCs. Notably, the FeS_2@RBCs retains similarly strong NIR absorption at 808 nm and 1064 nm between the original FeS_2 and FeS_2@RBCs, suggesting that the RBCs coating does not impair the NIR adsorption of the inner nanoparticles. In addition, SDS-PAGE protein analysis shows that almost all membrane protein bands of RBCs are successfully transferred to FeS_2@RBCs (Fig. 2j). Western blot assay also demonstrates that CD47 protein, known as specific "don't eat me" marker on RBCs, is observed at a near equivalent degree on RBCs and FeS_2@RBCs. Taken together, these above data verified that RBC membrane was successfully coated onto the FeS_2 nanoparticles. Furthermore, the suspension stability of FeS_2@RBCs in PBS is evaluated and the results show that the hydrodynamic sizes of FeS_2@RBCs remain almost unchanged for 3 days in PBS, suggesting the favorable suspension stability of FeS_2@RBCs (Fig. S5).

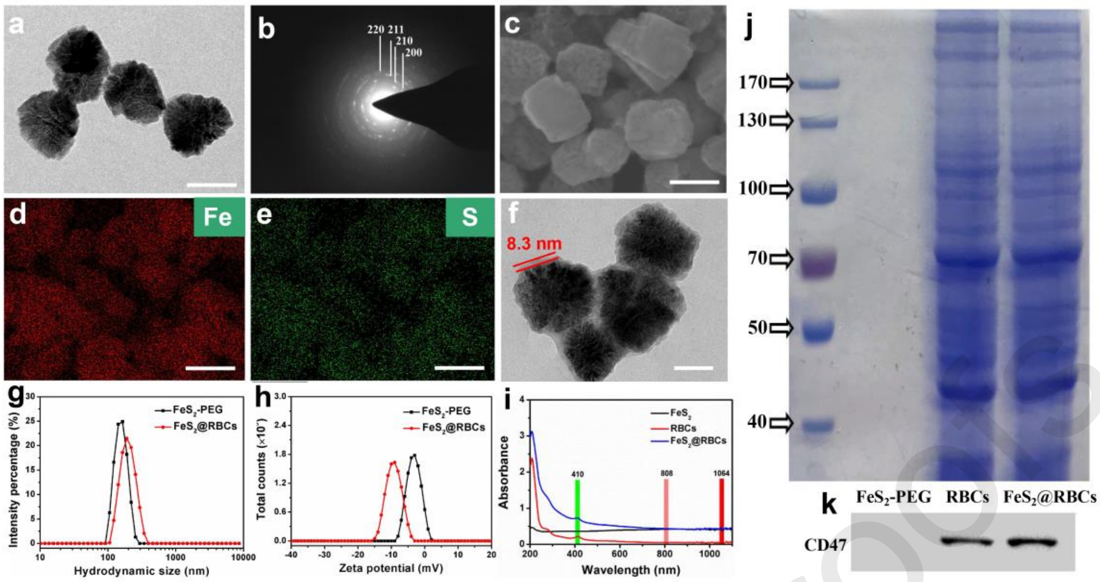

Fig. 2. Characterization of FeS_2, FeS_2-PEG and FeS_2@RBCs. (a) TEM image, (b) SAED pattern, (c) SEM image and (d,e) EDS element mapping of FeS_2, the scale bar indicates 100 nm. (f) TEM image of FeS_2@RBCs, the scale bar indicates 50 nm. (g) Hydrodynamic sizes and (h) zeta potentials of FeS_2-PEG and FeS_2@RBCs. (i) UV-vis spectra of FeS_2, RBCs and FeS_2@RBCs. (j) SDS-PAGE protein analysis of FeS_2-PEG, RBCs and FeS_2@RBCs. (k) Western blot analysis of FeS_2-PEG, RBCs and FeS_2@RBCs for characteristic RBCs marker CD47.

3.2 The photothermal effect of the FeS_2@RBCs

After confirming the successful fabrication of FeS_2@RBCs, the photothermal effects of the nanoparticles are investigated. As mentioned above, FeS_2@RBCs shows strong UV-vis adsorption at 1064 nm which belongs to the NIR-II window. Therefore, 1064 nm laser is firstly used to test the photothermal properties of FeS_2@RBCs. As shown in Fig. 3a, the temperature of FeS_2@RBCs solutions increases significantly with the irradiation of 1064 nm laser and a prominent temperature elevation of 25.3 ^{o}C is observed at a power density of clinical appoved 1.0 W/cm^2. Furthermore, a more remarkable temperature rise occurs with a higher FeS_2@RBCs concentrations (Fig. 3b).

The photothermal conversion efficiency of FeS_2@RBCs is calculated to be 30.2% according to the Roper's method [53]. The photostability tests of FeS_2@RBCs reveal that the maximum temperature and morphology does not show significant change under the repeated laser irradiation, which suggests that FeS_2@RBCs could serve as a stable PTT agent (Fig. S6 and Fig. S7). The photothermal performance of FeS_2-PEG and FeS_2@RBCs remains nearly unchanged, which indicates that the coating of FeS_2-PEG by RBC membrane does not impair the original photothermal property (Fig. S8). We also study the heating effects of FeS_2@RBCs treated with or without H_2O_2 since high concentration of H_2O_2 exists in tumor tissue [55]. As demonstrated in Fig. 3c, there is no significant change in the temperature rise of FeS_2@RBCs before and after H_2O_2 treatment, indicating that the possible self-oxidation caused by H_2O_2 in the TME will not impair the photothermal ability of FeS_2@RBCs. Moreover, the temperature rise of FeS_2@RBCs under 1064 nm laser illumination (1.0 W/cm^2, MPE for 1064nm laser) is significantly higher than that under 808 nm laser illumination (0.33 W/cm^2, MPE for 808 nm laser), as shown in Fig. 3d. Furthermore, we conduct an *in vivo* PTT study of FeS_2@RBCs by intratumor injection to further assess whether the PTT effect of FeS_2@RBCs with NIR-II laser of 1.0 W/cm^2 outperforms that with NIR-I laser of 0.33 W/cm^2. Upon NIR irradiation for 5 min, the tumor temperature of mice under 1064 nm laser irradiation increases rapidly to 49.6 ^{o}C, as compared to 43.2 ^{o}C for mouse treated with 808 nm laser (Fig. 3e). The above results reveal that FeS_2@RBCs exhibits excellent photothermal effect with NIR-II laser irradiation at the FDA-approved laser power density.

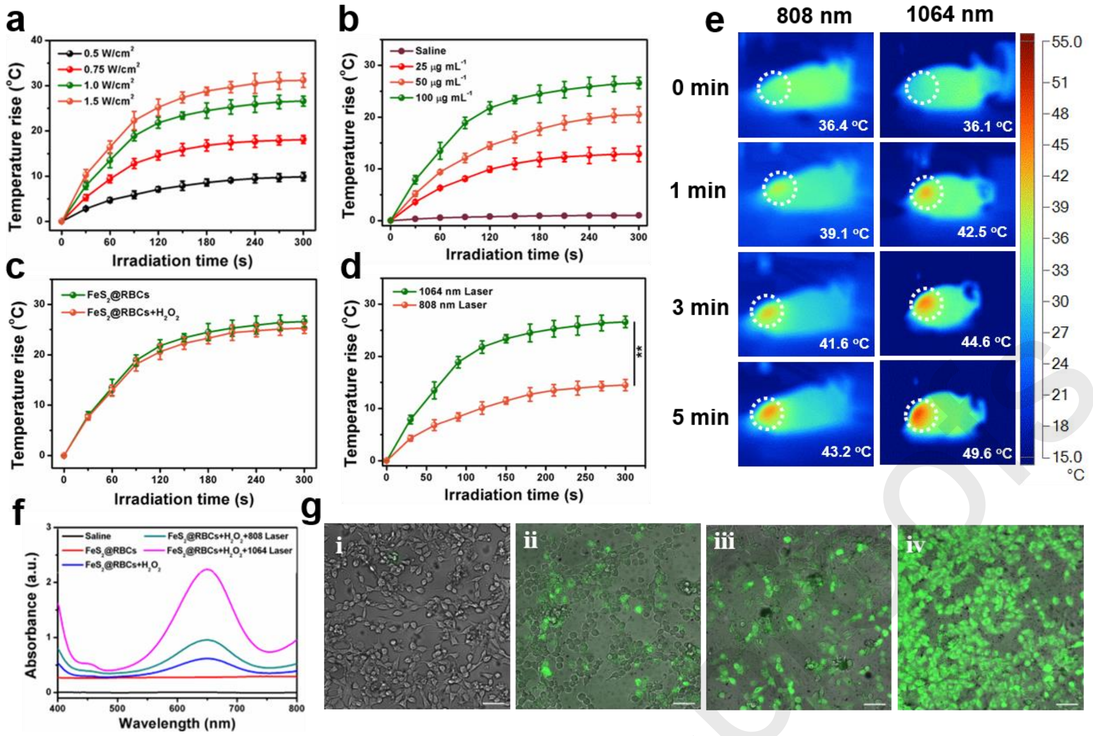

Fig. 3. *In vitro* and *in vivo* evaluation of the photothermal and chemodynamic effects of FeS_2@RBCs. (a) Temperature curves of FeS_2@RBCs (100 μg/mL) irradiated by different powder density of 1064 nm laser. (b) Temperature curves of FeS_2@RBCs with varied concentrations irradiated by 1064 nm laser (1.0 W/cm^2). (c) Temperature curves of FeS_2@RBCs (100 μg/ml) before and after treatment with H_2O_2 irradiated by 1064 nm laser (1.0 W/cm^2). (d) Temperature curve of FeS_2@RBCs (100 μg/ml) irradiated by 1064 nm laser (1.0 W/cm^2) or 808 nm laser (0.33 W/cm^2). (e) *In vivo* thermal photograph of 4T1 tumor-bearing mice by intratumor injection: left: FeS_2@RBCs+808 nm laser (0.33 W/cm^2, 5 min); right: FeS_2@RBCs+1064 nm laser (1.0 W/cm^2, 5 min). (f) Colorimetric analysis of the Fenton reaction for TMB decolorization of different groups. (g) Confocal images of ROS generation: i: Control, ii: FeS_2@RBCs, iii: FeS_2@RBC+808 nm laser (0.33 W/cm^2, 5 min) and iv: FeS_2@RBCs+1064 nm laser (1.0 W/cm^2, 5 min). 100 μM H_2O_2 is added in the groups. Scale bar indicates 50 μm. *p< 0.1, **p < 0.01, ***p < 0.001, and *n.s.* representing no significance. Data are means ±s.d.

3.3 The chemodynamic effect of the FeS_2@RBCs

It is known that ·OH radical production by the Fenton reaction strongly depends on the reaction temperature [32]. Thus, ·OH radical generation triggered by FeS_2@RBCs with or without NIR irradiation are systemically explored by using 3,3',5,5'-Tetramethylbenzidine dihydrochloride (TMB). In the presence of ·OH radicals, the colorless TMB could be oxidized into blue-green chromogenic TMB, which exhibits the characteristic UV absorption peak at 650 nm. As shown in Fig. 3f, the ·OH radical generation is enhanced in the presence of FeS_2@RBCs with H_2O_2 compared to FeS_2@RBCs without H_2O_2 group. Furthermore, after illumination with 808 nm laser (0.33 W/cm^2), the absorbance intensity of TMB is slightly higher than that without laser illumination, because of the mild temperature rise (Fig. 3f). Notably, a strongest absorbance intensity of TMB is observed after irradiation with 1064 nm laser (1.0 W/cm^2), suggesting that the chemodynamic effect of FeS_2@RBCs is significantly accerlerated with 1064 nm laser irradiation. In addition, the experiment of ·OH radical generation at different pH values is performed by MB decolorization with the addition of FeS_2@RBCs of 50 µg/ml and H_2O_2 of 100 µM. The characteristic UV absorption peak at 660 nm decreases with a lower pH value, which suggests that a low pH could accelerate the generation of ·OH radical (Fig. S9). To further verify the production of ·OH radical at the cellular level, DCFH-DA is used as a fluorescent probe to detect the intracellular ·OH radical level by CLSM imaging. Compared with other groups, 4T1 cells treated with FeS_2@RBCs followed by 1064 nm irradiation demonstrates the strongest green fluorescent signals with fluorescent intensity 2.41-fold higher than that of 808 nm irradiation, indicating that the hyperthermia generated by FeS_2@RBCs under

1064 nm laser irradiation could effectively improve the production efficiency of ·OH radical (Fig. 3g and Fig. S10**)**. The FeS_2@RBCs is intratumorally injected into the tumors with different treatment and the generation of ·OH radical is characterized by DCFH-DA staining. The results show that FeS_2@RBCs leads to a modest green fluorescent whereas a stronger green fluorescent is observed with the irradiation of 808 nm laser. Furthermore, the strongest green fluorescent is found in the group of FeS_2@RBCs+1064 nm laser, suggesting that the injection of FeS_2@RBCs with 1064 nm laser irradiation could effectively induce the generation of ·OH radical in tumor tissue (Fig. S11). Taken together, hyperthermia caused by FeS_2@RBCs under 1064 nm laser irradiation at the FDA-approved laser power could greatly promote the ·OH radical generation, which allows us to apply FeS_2@RBCs for HPTT-enhanced CDT *in vitro*.

3.4 In vitro cytotoxicity of FeS_2@RBCs

Firstly, 293T cells and 4T1 cells are applied to assess the intrinsic cytotoxicity of FeS_2@RBCs by CCK-8. Fig. 4a reveals that FeS_2@RBCs exhibits no remarkable cytotoxicity against both 293T and 4T1 cells up to 200 μg/mL after 24 h of incubation, indicating the favorable biosafety of FeS_2@RBCs. Then, we explore the cellular uptake behavior of FeS_2@RBCs by 4T1 cells. It is found that FeS_2@RBCs could enter into the 4T1 cells effectively with the extension of incubation time (Fig. S12). Based on the good chemodynamic property of FeS_2@RBCs mentioned above, we assess the CDT effect of FeS_2@RBCs on 4T1 cancer cell in the presence of tumor H_2O_2 level. It is found that the cancer cell inhibition rates are highly dependent on both FeS_2@RBCs and H_2O_2 concentrations (Fig. 4b). In the presence of H_2O_2, FeS_2@RBCs presents significant cell growth inhibition, due to the generation of highly toxic ·OH radical. Afterwards, we assess the PTT enhanced CDT effect of FeS_2@RBCs on 4T1 cell under the NIR laser irradiation. As shown in Fig. 4c, the inhibition rate of 4T1 cells treated with 1064 nm laser irradiation is superior than that of 808 nm laser irradiation, due to the better photothermal effect by 1064 nm laser. Furthermore, the living and dead cells are observed with Calcein-AM/PI staining by using CLSM. The CLSM results further confirm that the introduction of FeS_2@RBCs with 1064 nm laser irradiation and the addition of H_2O_2 leads to the most remarkable 4T1 cell death compared to other groups, which indicates the excellent synergistic PTT and CDT antitumor effect under NIR-II laser (Fig. 4d and Fig. S13) [32,35,38].

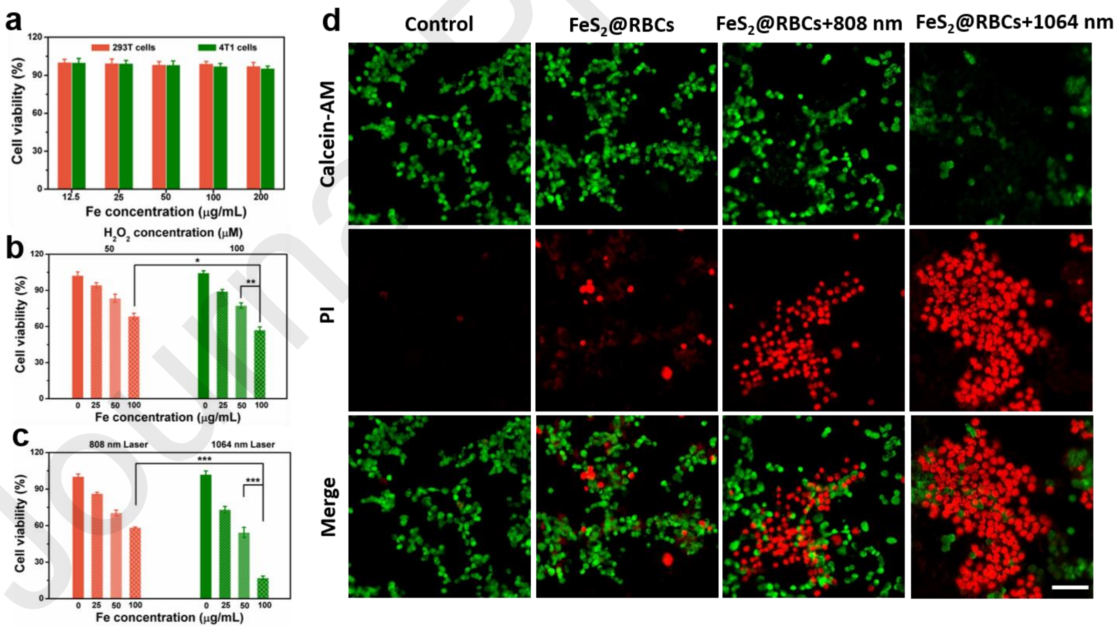

Fig. 4. *In vitro* evaluation of the PTT and PTT enhanced CDT effect. (a) the cell viability of 293T and 4T1 cells incubation with different concentration of FeS_2@RBCs; (b) The CDT effect of FeS_2@RBCs with different concentrations of H_2O_2 on 4T1 cells; (c) The PTT enhanced CDT effect of FeS_2@RBCs under the irradiation of 808 nm laser (0.33 W/cm^2, 5 min) or 1064 nm laser (1.0 W/cm^2, 5 min); (d) Fluorescence confocal

microscopy images of 4T1 cells stained with PI and Calcein-AM after incubation with FeS_2@RBCs under the irradiation of 808 nm laser (0.33 W/cm^2, 5 min) or 1064 nm laser (1.0 W/cm^2, 5 min). 100 μM H_2O_2 is added in the groups. Red channel images are obtained from PI ($\lambda_{ex}/\lambda_{em}$, 535/617 nm) while green channel images are obtained from Calcein-AM ($\lambda_{ex}/\lambda_{em}$, 495/515 nm). Scale bar indicates 50 μm. *p< 0.1, **p < 0.01, ***p < 0.001, and *n.s.* representing no significance. Data are means ±s.d.

3.5 Lipidomics analysis

It is well known that free radicals are prone to react with the biomacromolecules *in vivo* including lipids, proteins, and genetic materials [56]. Lipids, as an significant part of cell membranes, play a crucial role in keeping cell structure and providing signal transduction functions [57]. In this work, LC-MS is applied to compare the differences of cell lipid levels with or without free radicals between Laser(-) group (FeS_2@RBCs without laser irradiation) and Laser(+) group (FeS_2@RBCs with 1064 nm laser irradiation). After data pretreatment, 532 lipid molecules are detected by searching the Lipid Map database, and the annotated lipids are classified into 22 categories according to the lipid chains and groups (Fig. 5a). Principal component analysis (PCA) is employed to analyze the detected lipid molecules, which exhibits that the Laser (+) group is gathered in the positive direction while Laser (-) group is gathered in the negative direction (Fig. 5b). Meanwhile, partial least squares-discriminant analysis (PLS-DA) is performed and the results also exhibit that the Laser (-) and Laser (+) groups could be separated, which agrees well with the PCA result (Fig. S14). Furthermore, the relative values of lipids with different treatments are analyzed by hierarchical clustering, and the relative upregulation (red) or downregulation (green) of lipid concentration in different groups are displayed by a thermogram (Fig. 5c). Notably, Lipids of polyunsaturated fatty acids (PUFAs) with unstable diallyl hydrogen atoms are highly susceptible to lipid peroxidation. The proportion of PUFAs in subspecies lipids with or without laser irradiation is compared. Meanwhile, the difference of subspecies lipids is exhibited by a box diagram. Phosphatidylcholines (PC) and phosphatidylserines (PS) with arachidonic acid are more prone to be oxidized. It is found that the proportion of PUFAs such as LPC (18:1), LPC (19:0), PC (33:1e), PC (33:1D3), PS (39:1), and PS (40:6) relatively diminished (Fig. 5d,e and S15a-f). The propotion of Cer and CL are also analyzed and the results show that the content of PUFAs in Cer (d30:0) and CL (78:7) decreases as well (Fig 5f,g and S15g,h). At last, the correlation of different lipids is studied, which reveals that the lipid metabolites of similar types are distributed in the same cluster with similar trends (Fig S16). The above results demonstrate that cytotoxicity is related to free radical-mediated lipid damage by CDT which is augmented by the NIR-II laser irradiation.

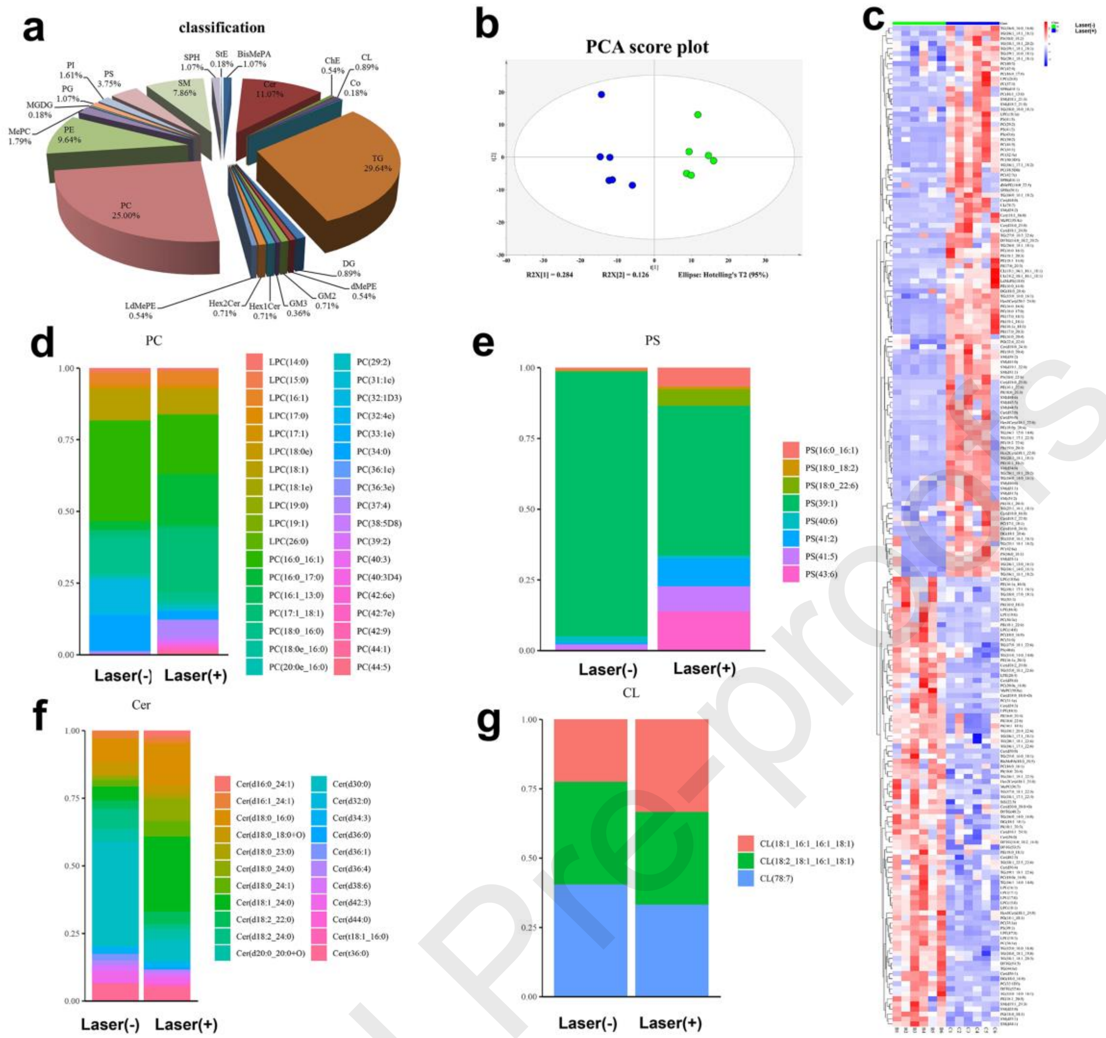

Fig. 5. Lipidomics analysis. (a) Classification of the 4T1 cell lipids by the biological process. (b) PCA score plot from the analysis of LC-MS spectra of 4T1 cells treated with FeS_2@RBCs irradiated by 1064 nm laser or not. Laser(-): no laser irradiation; Laser(+): laser irradiation (1.0 W/cm^2, 5 min). (FeS_2@RBCs: 100 μg/mL, n = 6) (c) The relative values of lipids with different treatments (Laser(-) or Laser(+)) as the metabolic level, hierarchical clustering analysis is performed, and the results are exhibited by a heat map. The relative content is presented by color differences, with columns representing samples and rows representing lipids. (d-g) Lipids are selected for biomarkers, and the sublipid content in four main kinds of differential lipids (PC, PS, Cer, and CL) are statistically analyzed.

3.6 In vivo pharmacokinetics, immune response and biodistribution evaluation

The blood circulation behavior of Cy5 modified FeS_2@RBCs is explored by tracing the fluorescent signals in blood. The Balb/c mice are received the first injection of Cy5 modified FeS_2-PEG or FeS_2@RBCs at the first day and the second injection at 7th days, respectively. The bloods are collected at different time points and the nanoparticle concentrations are quantitatively measured by a microplate reader. As demonstrated in Fig. 6a, FeS_2@RBCs displays significantly prolonged blood circulation with the elimination half-life ($t_{1/2}$) of 32.1 h as well as a blood retention of 22.3% ID/g at 24 h post-injection, whereas FeS_2-PEG shows a rapid clearance out of blood stream with the $t_{1/2}$ of 11.5 h and has only 10.1% ID/g blood retention at the same time point (Table. S1). Furthermore, regarding the second injection of FeS_2@RBCs at 7th days after the first injection, similar pharmacokinetic tendencies of FeS_2@RBCs is observed over 48h with the $t_{1/2}$ of 31.4 h, suggesting that no accelerated blood clearance (ABC) phenomenon is detected in the group of FeS_2@RBCs (Fig. 6b). However, the second injection of FeS_2-PEG performs significantly decreased blood circulation with a reduced $t_{1/2}$ of 6.2 h. The above results indicate that FeS_2@RBCs exhibit superior blood circulation than FeS_2-PEG, which is favorable for the higher tumor accumulation.

To investigate the potential mechanism for the different pharmacokinetic profiles between FeS_2@RBCs and FeS_2-PEG, we further test the IgM and IgG levels in mice serum after the first and second injection of nanoparticles, respectively. Fig. 6c displays that the IgM levels of FeS_2-PEG is 2.45-fold higher than that of FeS_2@RBCs, whereas FeS_2@RBCs shows no significant difference compared with the control group. Moreover, the IgG levels of FeS_2-PEG is 3.88-fold higher than that of FeS_2@RBCs, whereas FeS_2@RBCs shows no significant difference compared with the control group (Fig. 6d). Therefore, the repeated injection of FeS_2@RBCs will not induce the immune response which is favorable for the biomedical applications.

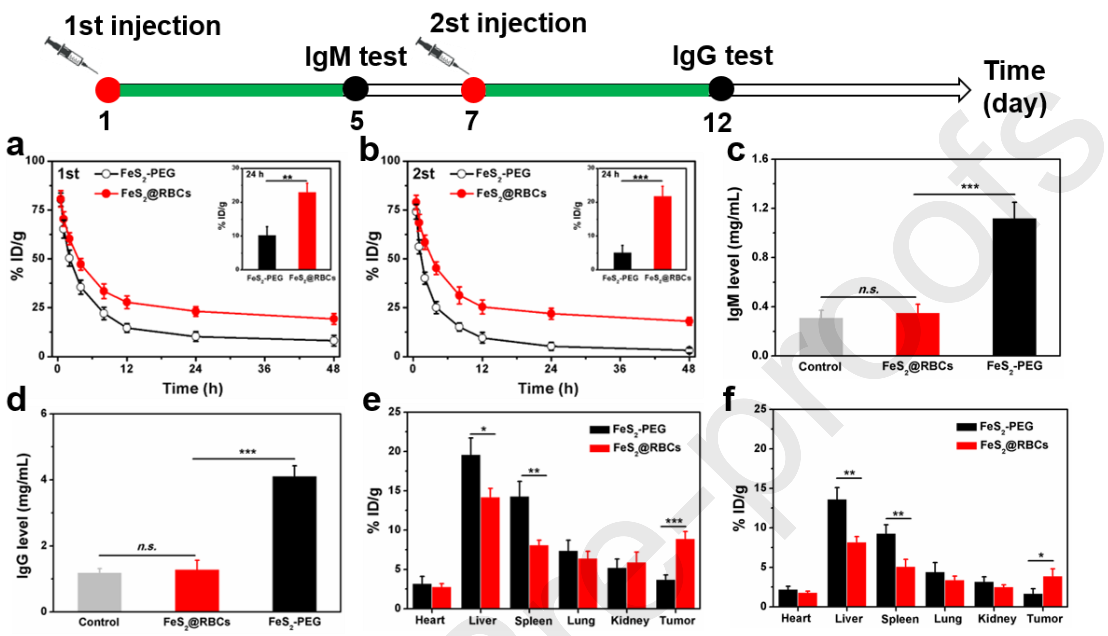

Fig. 6. Pharmacokinetic, immune response and biodistribution of FeS_2@RBCs. Blood retentions of FeS_2@RBCs and FeS_2-PEG for the first injection (a) and the second injection (b). (c) IgM level in blood serum at the 5th day after the first injection of nanoparticles (n=5). (d) IgG level in blood serum at the 5th day after the second injection of nanoparticles (n=5). Biodistribution of FeS_2@RBCs and FeS_2-PEG *in vivo* at 6 h (e) and 24 h (f) post injection. *$P < 0.1$, **$P < 0.01$, ***$P < 0.001$, and *n.s.* represents no significance.

Furthermore, the biodistribution evaluation of FeS_2@RBCs on 4T1 tumor-bearing mice is conducted. As shown in Fig. 6e and f, FeS_2@RBCs group achieves significant higher tumor accumulation with 8.7 % ID/g post-injection for 6 h compared with 4.2 % ID/g of FeS_2-PEG at the same time points. Furthermore, the tumor accumulation of FeS_2@RBCs post-injection for 24 h is also higher than that of FeS_2-PEG, which is attributed to the superior blood circulation of FeS_2@RBCs compared with FeS_2-PEG.

As the important metabolic organs in human body, liver and spleen could rapidly clear the foreign substances by phagocyte. Fig. 6e and f uncover that FeS_2@RBCs shows significant lower uptake by liver and spleen compared with FeS_2-PEG, indicating that RBCs coating renders FeS_2@RBCs with the immune evasion capabilities. Taken together, the above results demonstrate that FeS_2@RBCs achieves improved tumor accumulation and reduced uptake by liver and spleen, which may be beneficial for the enhanced PTT and CDT.

3.7 The self-enhanced MRI and near infrared fluorescence (NIFR) imaging

To evaluate the potential self-enhanced T_2-weighted MRI capability of FeS_2@RBCs, the transverse relaxation rates of FeS_2@RBCs solutions with varied concentrations of Fe treated with H_2O_2 or not are measured with a clinical MR scanner. As shown in Fig. 7a and b, the r_2 relaxivity of FeS_2@RBCs is calculated to be 30.6 $mM^{-1}\ s^{-1}$ after reacting with 100 μM of H_2O_2, whereas the r_2 relaxivity is only 6.2 $mM^{-1}\ s^{-1}$ without H_2O_2 treatment, due to the oxidation of FeS_2@RBCs in the presence of H_2O_2. Given that tumor region exhibits significant higher concentration of H_2O_2 compared with normal tissue, the TME-enhanced MRI of FeS_2@RBCs can be used for tumor specific detection and imaging-guided PTT. To further assess the feasibility of FeS_2@RBCs as a TME-enhanced contrast agent *in vivo*, FeS_2@RBCs is applied for tumor imaging in 4T1 tumor-bearing mice. First of all, FeS_2@RBCs is imaged with intratumor injection to explore the MRI signal change in TME. Fig. 7c reveals that the T_2 signal intensity of the tumor decreases gradually after the injection, which indicates the TME-enhanced ability of FeS_2@RBCs. Furthermore, the relative T_2 signal ratio of tumor declines approximately to 32.0 % after injection for 120 min compared with that of 0 min (Fig. S17). The decreased T_2 signal ratio can reasonably be ascribed to the self-oxidation of FeS_2@RBCs triggered by the overproduced H_2O_2 in TME. Furthermore, we continue to test the MRI performance of FeS_2@RBCs at tumor tissue *via* intravenous injection. As shown in Fig. 7d, the negative contrast enhancement of T_2 signal in tumor sites is also observed, and MRI T_2 signals reach the lowest post-injection for 6 h (Fig. S18). Therefore, FeS_2@RBCs, as a TME-enhanced contrast agent, could be applied to monitor the accumulation of FeS_2@RBCs and used for the imaging guided PTT.

To further investigate the tumor accumulation of FeS_2@RBCs, 4T1 tumor-bearing mice are intravenous injected with equivalent Cy5 modified FeS_2@RBCs or FeS_2-PEG for *in vivo* NIFR imaging. The fluorescent signal changes of FeS_2@RBCs and FeS_2-PEG at designated time points are shown in Fig. 7e. The FeS_2@RBCs displays strong fluorescent signals in tumor region, whereas FeS_2-PEG only exhibits mild fluorescence signal, which indicates that FeS_2@RBCs shows superior tumor accumulation compared with FeS_2-PEG. Notably, FeS_2@RBCs shows the most prominent fluorescent intensity which is 5.3-fold higher than that of FeS_2-PEG post-injection for 6 h (Fig. S19). After 6 h post-injection, the major organs (heart, liver, spleen, lung and kidney) and tumors of mice are harvested for *ex vivo* fluorescent imaging. In line with the *in vivo* fluorescent imaging, remarkable fluorescent signals are observed in tumor region in FeS_2@RBCs group, whereas fluorescent signals are focused in liver in FeS_2-PEG group (Fig. 7e). The CLSM images of tumor slice demonstrate the strong red signal of Cy5 in tumor region, which confirms the successful delivery of FeS_2@RBCs to the tumor region (Fig.

7f). The above results reliably indicate that the RBCs coating significantly improve the blood circulation and enhance the tumor accumulation, which is beneficial for the PTT effect of FeS_2@RBCs with a low power of NIR-II laser.

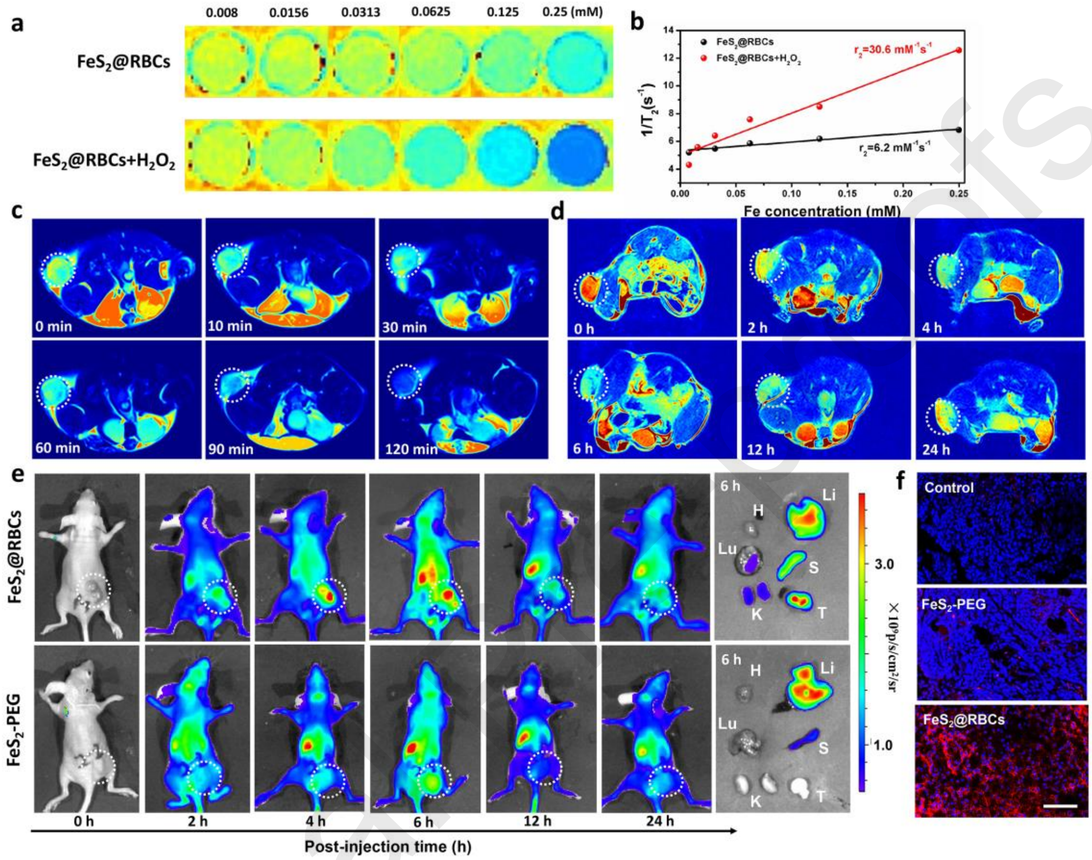

Fig. 7. TME-enhanced MRI and NIRF imaging tumor injection with FeS_2@RBCs. (a) T_2-weighted MR images and the corresponding transverse relaxation rates (b) of the FeS_2@RBCs treated with H_2O_2 (100 μM) or not. (c) T_2-weighted MR images of 4T1 tumor-bearing nude mice at different time points before and after intra-tumoral injection with FeS_2@RBCs. (d) T_2-weighted MR images of 4T1 tumor-bearing nude mice at different time points before and after intravenous injection with FeS_2@RBCs. (e) NIRF images of 4T1 tumor-bearing nude mice at different time points before and after intravenous injection with Cy5 modified FeS_2@RBCs and FeS_2-PEG, and *ex vivo* NIRF images of major organs and tumors harvested from the 4T1 tumor-bearing mice at 6 h post injection. White circles: tumor sites. (f) Confocal images of the tumor tissues

harvested from the 4T1 tumor-bearing mice at 6 h post injection. DAPI-stained nuclei, Cy5 are shown in red. Scale bar: 100 μm.

Encouraged by the PTT augmented CDT effects *in vitro*, the anti-tumor experiments *in vivo* are then performed on 4T1 tumor models. Six groups are included: saline, FeS_2-PEG, FeS_2@RBCs, FeS_2-PEG (++), FeS_2@RBCs (+) and FeS_2@RBCs (++) (n = 5 per group). (+) indicates 808 nm laser irradiation (0.33 W/cm^2) for 5 min and (++) indicates 1064 nm laser irradiation (1.0 W/cm^2) for 5 min. Six groups of 4T1-bearing mice are then i.v. injected with 0.1 mL of saline or nanoparticle dispersions (3 mg Fe/kg) with the tumor volume of 100 mm^3. In the laser irradiation groups, the tumor region of mice is irradiated by the NIR laser for 300 s at 6 h after injection. The thermal images of tumor region are obtained at different time intervals and the tumor local temperature rises to 36.7 ^oC, 38.8 ^oC and 45.3 ^oC for the group of FeS_2-PEG (++), FeS_2@RBCs (+) and FeS_2@RBCs (++), respectively (Fig. S20). The tumor growth curves show that FeS_2-PEG group shows slight tumor growth inhibition because of the mild CDT effect (Fig. 8a). Furthermore, the tumor growth inhibition is enhanced because of the improved tumor accumulation of FeS_2@RBCs. Among all of the groups, FeS_2@RBCs (++) displays the smallest tumor volume, due to the enhanced HPTT augmented CDT effects (Fig. 8b). The tumor weight in Fig. 8c also disclose the same trend similar as tumor volume inhibition, suggesting that FeS_2@RBCs could effectively treat 4T1 cancer by HPTT augmented CDT with a clinical approved 1064 nm laser. Meanwhile, *in situ* TUNEL analysis exhibits that the most cell apoptosis is observed in the FeS_2@RBCs (++) group and HE staining also reveals the most prominent inhibition of tumor cells (Fig. 8e). The above results are supportive of the best antitumor efficacy of FeS_2@RBCs (++) among all the treatment groups.

To test the biosafety of the FeS_2@RBCs, mice are sacrificed 14 days after different treatment, with major organs collected and sliced for histology analysis. No significant tissue damages to the main organs are found for each group, suggesting the favorable biocompatibility of FeS_2@RBCs (Fig. S21). At the meantime, no obvious body weight loss (Fig. 8d) are found for all the treatment groups, which indicates the favorable bio-safety of the FeS_2@RBCs. The blood biochemistry assay is performed to explore the long-term safety of FeS_2@RBCs. The results show no significant difference is found among the mice between the PBS group and FeS_2@RBCs group, suggesting that FeS_2@RBCs shows favorable biocompatibility and biosafety (Fig. S22). Therefore, the above results demonstrate that FeS_2@RBCs exhibits no significant toxicity *in vivo*.

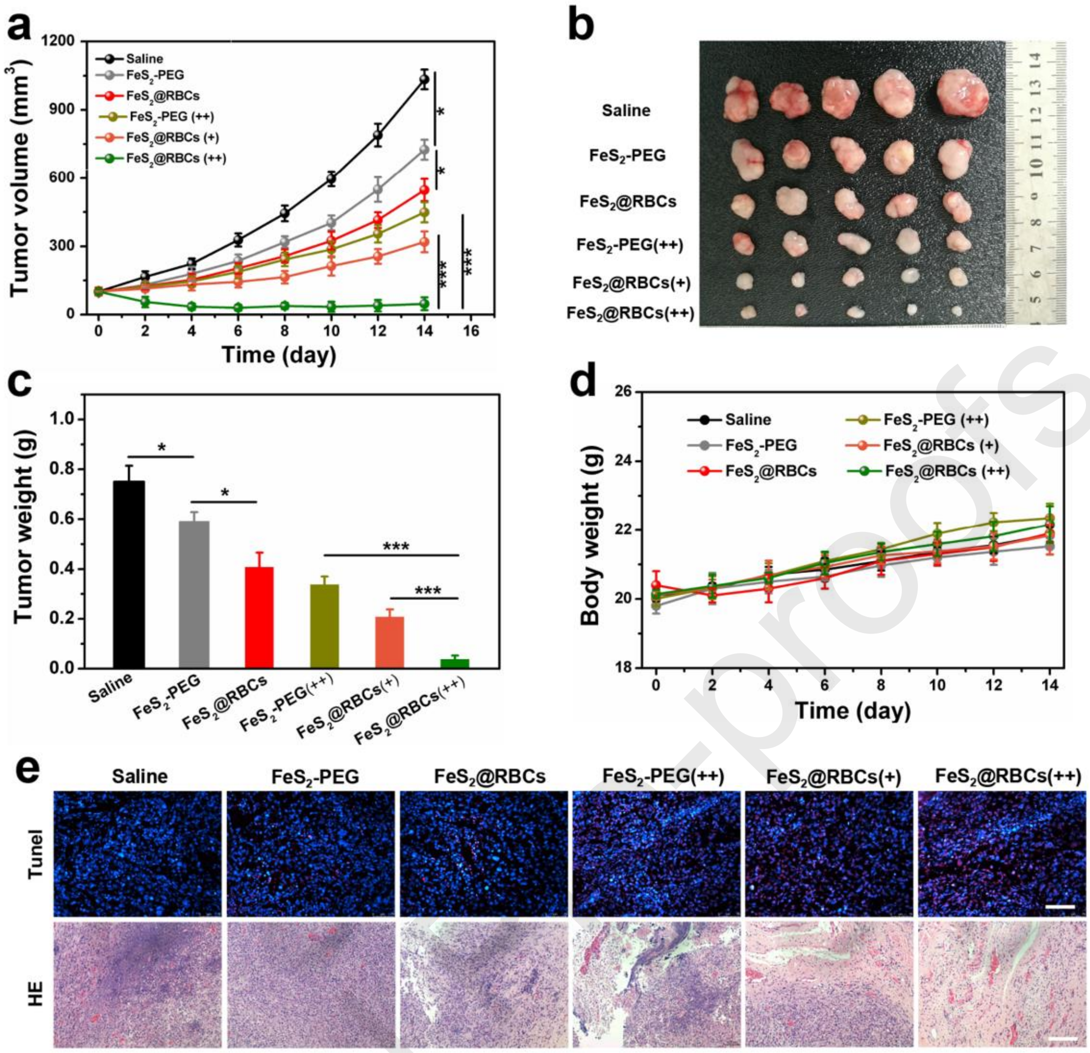

Fig 8. *In vivo* PTT and CDT effects of FeS_2@RBCs. (a) Tumor volume curves of 4T1 tumor-bearing mice with different treatments. (b) Photographs of tumors from different groups and (c) tumor weights of each group after laser treatment. (d) Body weight curves of mice in each group observed for 14 days. (e) TUNEL and HE staining of tumor tissues 14 days after different treatments. (+) indicates 808 nm laser irradiation (0.33 W/cm^2) for 5 min and (++) indicates 1064 nm laser irradiation (1.0 W/cm^2) for 5 min. Nuclei and apoptotic cells are stained blue and red, respectively. The scale bar is 75 μm. *p< 0.1, **p < 0.01, ***p < 0.001, and *n.s.* representing no significance. Data are means ±s.d. N=5.

4. Conclusion

In summary, we have successfully developed red blood cell membranes (RBCs) coated FeS_2 (FeS_2@RBCs) for HPTT augmented CDT with a clinical approved 1064 nm laser. FeS_2@RBCs with strong absorption at the NIR-II window exhibits excellent photothermal efficiency under 1064 nm irradiation at 1.0 W/cm^2 (FDA approved power density). Furthermore, the RBCs coating provides the nanoparticles with prolonged blood circulation and negligible immune response, thus improving the tumor accumulation for enhanced HPTT. Importantly, hyperthemia in the tumor region simultaneous augments the CDT effect of FeS_2@RBCs, which leads to the HPTT-enhanced CDT with NIR-II laser irradiation. Additionally, FeS_2@RBCs exhibits self-enhanced MRI after reacting with the overproduced H_2O_2 in tumor region for imaging-guided HPTT. The synergetic HPTT and CDT are comprehensively demonstrated both *in vitro* and *in vivo*. This work provides a HPTT augmented CDT strategy for effective cancer therapy with a clinical approved laser power, which may pave the way for the clinical application of synergetic HPTT and CDT in the future.

Notes

The authors declare no competing financial interest.

Acknowledgements

This work is financially supported by the National Natural Science Foundation of China (Grant Nos. 81903165, 81501435), the National Natural Science Foundation of Shanghai (Grant No. 18ZR1405700, 17411953700, and 16410722800).

Data availability statement

The data are available from the corresponding author (henry2008_ok@126.com) on reasonable request.

References

[1] L. Cheng, C. Wang, L. Feng, K. Yang, Z. Liu, Functional Nanomaterials for Phototherapies of Cancer, Chem. Rev. 114 (2014) 10869–10939.

[2] Y. Liu, P. Bhattarai, Z. Dai, X. Chen, Photothermal therapy and photoacoustic imaging via nanotheranostics in fighting cancer, Chem. Soc. Rev. 48 (2019) 2053–2108.

[3] X. Zhen, C. Xie, K. Pu, Temperature-Correlated Afterglow of a Semiconducting Polymer Nanococktail for Imaging-Guided Photothermal Therapy, Angew. Chem. Int. Ed. 57 (2018) 3938–3942.

[4] Y. Yang, W. Zhu, Z. Dong, Y. Chao, L. Xu, M. Chen, Z. Liu, 1D Coordination Polymer Nanofibers for Low-Temperature Photothermal Therapy, Adv. Mater. 29 (2017) 1703588.

[5] J. Zhou, M. Li, Y. Hou, Z. Luo, Q. Chen, H. Cao, R. Huo, C. Xue, L. Sutrisno, L. Hao, Y. Cao, H. Ran, L. Lu, K. Li, K. Cai, Engineering of a Nanosized Biocatalyst for Combined Tumor Starvation and Low-Temperature Photothermal Therapy, ACS Nano 12 (2018) 2858–2872.

[6] K. Zhang, X. Meng, Y. Cao, Z. Yang, H. Dong, Y. Zhang, H. Lu, Z. Shi, X. Zhang, Metal–Organic Framework Nanoshuttle for Synergistic Photodynamic and Low-Temperature Photothermal Therapy, Adv. Funct. Mater. 28 (2018) 1804634.

[7] B. Ouyang, F. Liu, S. Ruan, Y. Liu, H. Guo, Z. Cai, X. Yu, Z. Pang, S. Shen, Localized Free Radicals Burst Triggered by NIR-II Light for Augmented Low-

Temperature Photothermal Therapy, ACS Appl. Mater. Interfaces 11 (2019) 38555–38567.

[8] W. Chen, J. Ouyang, H. Liu, M. Chen, K. Zeng, J. Sheng, Z. Liu, Y. Han, L. Wang, J. Li, L. Deng, Y.N. Liu, S. Guo, Black Phosphorus Nanosheet-Based Drug Delivery System for Synergistic Photodynamic/Photothermal/Chemotherapy of Cancer, Adv. Mater. 29 (2017) 1603864.

[9] G. Gao, Y.W. Jiang, W. Sun, Y. Guo, H.R. Jia, X.W. Yu, G.Y. Pan, F.G. Wu, Molecular Targeting-Mediated Mild-Temperature Photothermal Therapy with a Smart Albumin-Based Nanodrug, Small 15 (2019) e1900501.

[10] Z. Meng, F. Wei, W. Ma, N. Yu, P. Wei, Z. Wang, Y. Tang, Z. Chen, H. Wang, M. Zhu, Design and Synthesis of "All-in-One" Multifunctional FeS2 Nanoparticles for Magnetic Resonance and Near‐Infrared Imaging Guided Photothermal Therapy of Tumors, Adv. Funct. Mater. 26 (2016) 8231-8242.

[11] G. Liao, F. He, Q. Li, L. Zhong, R. Zhao, H. Che, H. Gao, B. Fang, Emerging graphitic carbon nitride-based materials for biomedical applications, Prog. Mater. Sci. 112 (2020) 100666.

[12] W. Guo, C. Guo, N. Zheng, T. Sun, S. Liu, CsxWO3 Nanorods Coated with Polyelectrolyte Multilayers as a Multifunctional Nanomaterial for Bimodal Imaging-Guided Photothermal/Photodynamic Cancer Treatment, Adv. Mater. 29 (2017) 1604157.

[13] H. Liu, Q. Yang, W. Guo, H. Lin, F. Zhang, J. Zhao, T. Ma, L. Zhao, N. Xu, R. Wang, J. Yu, F. Qu, CoWO4-x-based nanoplatform for multimode imaging and enhanced photothermal/photodynamic therapy, Chem. Eng. J. 385 (2020) 123979.

[14] D. De Luca, I. Delfino, M. Lepore, Laser safety standards and measurements of hazard parameters for medical lasers, Int J Opt Appl. 2 (2012) 80-86.

[15] ANSI Z136.1-2014, American National Standard For Safe Use Of Lasers, American National Standards Institute 2014.

[16] A. Bashkatov, E. Genina, V. Kochubey, V. Tuchin, Optical properties of human skin, subcutaneous and mucous tissues in the wavelength range from 400 to 2000 nm, J. Phys. D-Appl. Phys. 38 (2005) 2543.

[17] Y. Liu, W. Zhen, Y. Wang, J. Liu, L. Jin, T. Zhang, S. Zhang, Y. Zhao, S. Song, C. Li, J. Zhu, Y. Yang, H. Zhang, One-Dimensional Fe_2P Acts as a Fenton Agent in Response to NIR II Light and Ultrasound for Deep Tumor Synergetic Theranostics, Angew. Chem. Int. Edit. 58 (2019) 2407-2412.

[18] G. Liu, J. Zhu, H. Guo, A. Sun, P. Chen, L. Xi, W. Huang, X. Song, X. Dong, Mo_2C-Derived Polyoxometalate for NIR-II Photoacoustic Imaging-Guided Chemodynamic/Photothermal Synergistic Therapy, Angew. Chem. Int. Edit. 58 (2019) 18641-18646.

[19] J. Li, R. Jiang, Q. Wang, X. Li, X. Hu, Y. Yuan, X. Lu, W. Wang, W. Huang, Q. Fan, Semiconducting polymer nanotheranostics for NIR-II/Photoacoustic imaging-guided photothermal initiated nitric oxide/photothermal therapy, Biomaterials 217 (2019) 119304.

[20] Y. Jiang, J. Li, X. Zhen, C. Xie, K. Pu, Dual-Peak Absorbing Semiconducting Copolymer Nanoparticles for First and Second Near-Infrared Window Photothermal Therapy: A Comparative Study, Adv. Mater. 30 (2018) 1705980.

[21] X. Wang, H. Li, X. Liu, Y. Tian, H. Guo, T. Jiang, Z. Luo, K. Jin, X. Kuai, Y. Liu, Z. Pang, W. Yang, S. Shen, Enhanced photothermal therapy of biomimetic polypyrrole nanoparticles through improving blood flow perfusion, Biomaterials 143 (2017) 130-141.

[22] J.G. Piao, L. Wang, F. Gao, Y.Z. You, Y. Xiong, L. Yang, Erythrocyte membrane is an alternative coating to polyethylene glycol for prolonging the circulation lifetime of gold nanocages for photothermal therapy, ACS Nano 8 (2014) 10414-10425.

[23] X. Ren, R. Zheng, X. Fang, X. Wang, X. Zhang, W. Yang, X. Sha, Red blood cell membrane camouflaged magnetic nanoclusters for imaging-guided photothermal therapy, Biomaterials 92 (2016) 13-24.

[24] K. H, I. T, Accelerated blood clearance (ABC) phenomenon upon repeated injection of PEGylated liposomes, Int J Pharm. 354 (2008) 56-62.

[25] M.J. Webber, E.A. Appel, B. Vinciguerra, A.B. Cortinas, L.S. Thapa, S. Jhunjhunwala, L. Isaacs, R. Langer, D.G. Anderson, Supramolecular PEGylation of biopharmaceuticals, Proc. Natl. Acad. Sci. U. S. A. 113 (2016) 14189-14194.

[26] C.M. Hu, L. Zhang, S. Aryal, C. Cheung, R.H. Fang, L. Zhang, Erythrocyte membrane-camouflaged polymeric nanoparticles as a biomimetic delivery platform, Proc. Natl. Acad. Sci. U. S. A. 108 (2011) 10980-10985.

[27] Z. Chen, P. Zhao, Z. Luo, M. Zheng, H. Tian, P. Gong, G. Gao, H. Pan, L. Liu, A. Ma, H. Cui, Y. Ma, L. Cai, Cancer Cell Membrane-Biomimetic Nanoparticles for Homologous-Targeting Dual-Modal Imaging and Photothermal Therapy, ACS Nano 10 (2016) 10049-10057.

[28] Y. Zhang, K. Cai, C. Li, Q. Guo, Q. Chen, X. He, L. Liu, Y. Zhang, Y. Lu, X. Chen, T. Sun, Y. Huang, J. Cheng, C. Jiang, Macrophage-Membrane-Coated Nanoparticles for Tumor-Targeted Chemotherapy, Nano Lett. 18 (2018) 1908-1915.

[29] S. Peng, B. Ouyang, Y. Men, Y. Du, Y. Cao, R. Xie, Z. Pang, S. Shen, W. Yang, Biodegradable zwitterionic polymer membrane coating endowing nanoparticles with ultra-long circulation and enhanced tumor photothermal therapy, Biomaterials 231 (2020) 119680.

[30] L. Rao, L.L. Bu, J.H. Xu, B. Cai, G.T. Yu, X. Yu, Z. He, Q. Huang, A. Li, S.S. Guo, W.F. Zhang, W. Liu, Z.J. Sun, H. Wang, T.H. Wang, X.Z. Zhao, Red Blood Cell Membrane as a Biomimetic Nanocoating for Prolonged Circulation Time and Reduced Accelerated Blood Clearance, Small 11 (2015) 6225-6236.

[31] P.A. Oldenborg, A. Zheleznyak, Y.F. Fang, C.F. Lagenaur, H.D. Gresham, F.P. Lindberg, Role of CD47 as a marker of self on red blood cells, Science 288 (2000) 2051-2054.

[32] Z. Tang, Y. Liu, M. He, W. Bu, Chemodynamic Therapy: Tumour Microenvironment-Mediated Fenton and Fenton-like Reactions, Angew. Chem. Int. Ed. 58 (2019) 946-956.

[33] C. Liang, X. Zhang, M. Yang, X. Dong, Recent Progress in Ferroptosis Inducers for Cancer Therapy, Adv. Mater. 31 (2019) e1904197.

[34] C. Zhang, W. Bu, D. Ni, S. Zhang, Q. Li, Z. Yao, J. Zhang, H. Yao, Z. Wang, J. Shi, Synthesis of Iron Nanometallic Glasses and Their Application in Cancer Therapy by a Localized Fenton Reaction, Angew. Chem. Int. Ed. 55 (2016) 2101-2106.

[35] M. Zhang, B. Sheng, J. Ashley, T. Zheng, W. Wang, Q. Zhang, J. Zhang, N. Zhou, J. Shen, Y. Sun, Manganese ion chelated FeOCl@PB@PDA@BPQDs nanocomposites as a tumor microenvironment-mediated nanoplatform for enhanced tumor imaging and therapy, Sens. Actuator B-Chem. 307 (2020) 127491.

[36] M. Huo, L. Wang, Y. Chen, J. Shi, Tumor-selective catalytic nanomedicine by nanocatalyst delivery, Nat. Commun. 8 (2017) 357.

[37] Y. Deng, J.D. Englehardt, Treatment of landfill leachate by the Fenton process, Water Res. 40 (2006) 3683-3694.

[38] G. Guan, X. Wang, B. Li, W. Zhang, Z. Cui, X. Lu, R. Zou, J. Hu, "Transformed" Fe3S4 tetragonal nanosheets: a high-efficiency and body-clearable agent for magnetic resonance imaging guided photothermal and chemodynamic synergistic therapy, Nanoscale. 10 (2018) 17902–17911.

[39] J. Zheng, N. Muhanna, R. De Souza, H. Wada, H. Chan, M.K. Akens, T. Anayama, K. Yasufuku, S. Serra, J. Irish, C. Allen, D. Jaffray, A multimodal nano agent for image-guided cancer surgery, Biomaterials 67 (2015) 160-168.

[40] T. Ma, P. Zhang, Y. Hou, H. Ning, Z. Wang, J. Huang, M. Gao, "Smart" Nanoprobes for Visualization of Tumor Microenvironments, Adv. Healthc. Mater. 7 (2018) e1800391.

[41] J. Li, K. Pu, Semiconducting Polymer Nanomaterials as Near-Infrared Photoactivatable Protherapeutics for Cancer, Acc. Chem. Res. 53 (2020) 752–762.

[42] Y. Jiang, P.K. Upputuri, C. Xie, Z. Zeng, A. Sharma, X. Zhen, J. Li, J. Huang, M. Pramanik, K. Pu, Metabolizable Semiconducting Polymer Nanoparticles for Second Near-Infrared Photoacoustic Imaging, Adv. Mater. 31 (2019) 1808166.

[43] Y. Jiang, P.K. Upputuri, C. Xie, Y. Lyu, L. Zhang, Q. Xiong, M. Pramanik, K. Pu, Broadband Absorbing Semiconducting Polymer Nanoparticles for Photoacoustic Imaging in Second Near-Infrared Window, Nano Lett. 17 (2017) 4964–4969.

[44] L. Li, S. Fu, C. Chen, X. Wang, C. Fu, S. Wang, W. Guo, X. Yu, X. Zhang, Z. Liu, J. Qiu, H. Liu, Microenvironment-Driven Bioelimination of Magnetoplasmonic Nanoassemblies and Their Multimodal Imaging-Guided Tumor Photothermal Therapy, ACS Nano 10 (2016) 7094-7105.

[45] M. Wang, K. Deng, W. Lu, X. Deng, K. Li, Y. Shi, B. Ding, Z. Cheng, B. Xing, G. Han, Z. Hou, J. Lin, Rational Design of Multifunctional Fe@gamma-Fe2O3 @H-TiO2 Nanocomposites with Enhanced Magnetic and Photoconversion Effects for Wide Applications: From Photocatalysis to Imaging-Guided Photothermal Cancer Therapy, Adv. Mater. 30 (2018) e1706747.

[46] Y. Zou, F. Sun, C. Liu, C. Yu, M. Zhang, Q. He, Y. Xiong, Z. Xu, S. Yang, G. Liao, A novel nanotheranostic agent for dual-mode imaging-guided cancer therapy

based on europium complexes-grafted-oxidative dopamine, Chem. Eng. J. 357 (2019) 237–247.

[47] S. Aime, D.D. Castelli, S.G. Crich, E. Gianolio, E. Terreno, Pushing the sensitivity envelope of lanthanide-based magnetic resonance imaging (MRI) contrast agents for molecular imaging applications, Accounts Chem. Res. 42 (2009) 822-831.

[48] L. Zhang, R. Liu, H. Peng, P. Li, Z. Xu, A.K. Whittaker, The evolution of gadolinium based contrast agents: from single-modality to multi-modality, Nanoscale. 8 (2016) 10491–10510.

[49] Z. Gao, Y. Hou, J. Zeng, L. Chen, C. Liu, W. Yang, M. Gao, Tumor Microenvironment-Triggered Aggregation of Antiphagocytosis (99m) Tc-Labeled Fe_3O_4 Nanoprobes for Enhanced Tumor Imaging in vivo, Adv. Mater. 29 (2017) 1701095.

[50] Z. Shen, T. Chen, X. Ma, W. Ren, Z. Zhou, G. Zhu, A. Zhang, Y. Liu, J. Song, Z. Li, H. Ruan, W. Fan, L. Lin, J. Munasinghe, X. Chen, A. Wu, Multifunctional Theranostic Nanoparticles Based on Exceedingly Small Magnetic Iron Oxide Nanoparticles for T_1-Weighted Magnetic Resonance Imaging and Chemotherapy, ACS Nano 11 (2017) 10992-11004.

[51] Z. Tang, H. Zhang, Y. Liu, D. Ni, H. Zhang, J. Zhang, Z. Yao, M. He, J. Shi, W. Bu, Antiferromagnetic Pyrite as the Tumor Microenvironment-Mediated Nanoplatform for Self-Enhanced Tumor Imaging and Therapy, Adv. Mater. 29 (2017) 1701683.

[52] Q. Jiang, Y. Liu, R. Guo, X. Yao, S. Sung, Z. Pang, W. Yang, Erythrocyte-cancer hybrid membrane-camouflaged melanin nanoparticles for enhancing photothermal therapy efficacy in tumors, Biomaterials 192 (2019) 292-308.

[53] D.K. Roper, W. Ahn, M. Hoepfner, Microscale Heat Transfer Transduced by Surface Plasmon Resonant Gold Nanoparticles, J. Phys. Chem. C. Nanomater. Interfaces. 111 (2007) 3636–3641.

[54] Y. Lyu, C. Xie, S.A. Chechetka, E. Miyako, K. Pu, Semiconducting Polymer Nanobioconjugates for Targeted Photothermal Activation of Neurons, J. Am. Chem. Soc. 138 (2016) 9049–9052.

[55] Q. Chen, C. Liang, X. Sun, J. Chen, Z. Yang, H. Zhao, L. Feng, Z. Liu, H_2O_2-responsive liposomal nanoprobe for photoacoustic inflammation imaging and tumor theranostics via in vivo chromogenic assay. Proc. Natl. Acad. Sci. U. S. A. 114 (2017), 5343-5348.

[56] S. Daum, M. S. V. Reshetnikov, M. Sisa, T. Dumych, M. D. Lootsik, R. Bilyy, E. Bila, C. Janko, C. Alexiou, M. Herrmann, L. Sellner, A. Mokhir, Lysosome-Targeting Amplifiers of Reactive Oxygen Species as Anticancer Prodrugs. Angew. Chem., Int. Ed. 56 (2017) 15545-15549.

[57] L. S. Lin, T. Huang, J. Song, X. Y. Ou, Z. Wang, H. Deng, R. Tian, Y. Liu, J. F. Wang, Y. Liu, G. Yu, Z. Zhou, S. Wang, G. Niu, H. H. Yang, X. Chen, Synthesis of Copper Peroxide Nanodots for H_2O_2 Self-Supplying Chemodynamic Therapy. J. Am. Chem. Soc. 141 (2019) 9937-9945.

Declaration of interests

☒ The authors declare that they have no known competing financial interests or personal relationships that could have appeared to influence the work reported in this paper.

☐The authors declare the following financial interests/personal relationships which may be considered as potential competing interests:

Schematic illustrating the fabrication and anti-tumor effect of FeS_2@RBCs *in vivo*. With RBCs coating, FeS_2@RBCs exhibits prolonged blood circulation, which leads to the improved tumor accumulation. FeS_2@RBCs shows TME-enhanced MRI after reacting with H_2O_2 at tumor regions for imaging-guided HPTT. With a FDA approved 1064 nm laser, FeS_2@RBCs achieves effective HPTT, which significantly augments the CDT effects for tumor synergetic therapy. The growth of tumor could be significantly inhibited by a clinical approved NIR-II laser.

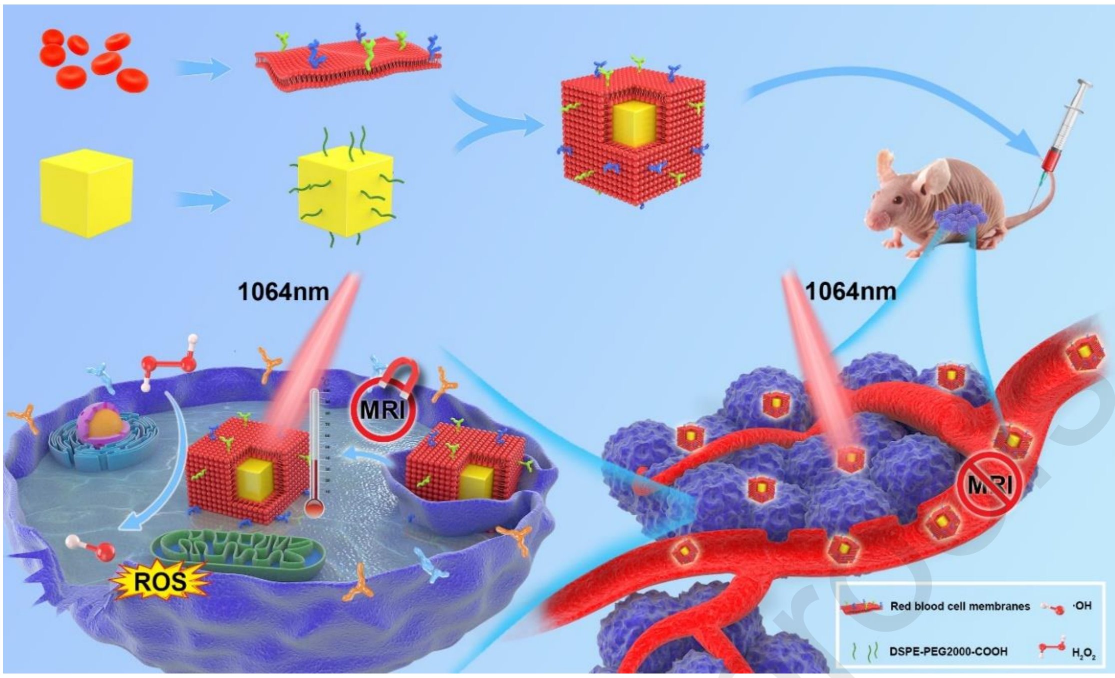

1. A biomimic FeS_2@RBCs with long blood circulation and negligible immune response is reported.
2. The obtained FeS_2@RBCs exhibits favorable hypothermal PTT with a clinical approved NIR-II light.
3. The chemodynamic effect of FeS_2@RBCs is significantly augmented by the PTT effect.
4. FeS_2@RBCs shows self-enhanced MRI to achieve the imaging guided PTT-CDT synergistic therapy.